Supplementary material

Ultrafast unidirectional on-chip heat transfer

Junbo Yang[a,b], Miao Liu[a,b], Tanhe Wang[a,b], Zhaoyang Wang[a,b], Chunsheng Guo[a,b,*], Keng-Te Lin[c], Han Lin[c,*], Baohua Jia[c,*]

[a] *School of Mechanical, Electrical and Information Engineering, Shandong University, Weihai 264209, China*

[b] *Suzhou Research Institute, Shandong University, 388 Ruoshui Road, Suzhou 215123, China*

[c] *School of Science, RMIT University, 124 La Trobe Street, Melbourne, Victoria 3000, Australia*

Supplementary Section 1: Structure optimization of valley photonic crystals

In this part, we discuss the optimization of the valley photonic crystal (VPC) structures. The reason for choosing the structure is that it exhibits a Dirac cone at the *K* (*K′*) point, and the dispersion of the valley Hall edge state contains two distinct regimes with opposite Chern numbers[1]. Furthermore, the topologically-protected edge states are required to operate below the light cone, ensuring the highly efficient transmission of thermal radiation with negligible out-of-plane radiation loss[2]. The VPC structures should operate in the infrared band (i.e., wavelength ranging from 7.5 μm to 9 μm) to dissipate heat according to the working temperature of electronic components. Therefore, one criterion of the optimization process is the working band. Besides, considering efficient heat dissipation, we maximize the output heat flux in the interested band.

Optimization of the structure is studied as a function of two parameters: the lattice constant a and the difference in diameter of circular air holes Δd. We design multiple structures with various a and Δd to guarantee that the photonic bandgap overlaps the interested working bandwidth (from 7.5 μm to 9 μm), and the detailed structural parameters are shown in Fig. S1(a). The band structure of transverse electric (TE) modes of VPC is calculated using the plane wave expansion (PWE) method. Importantly, the air holes in the structure maximize the refractive-index contrast between the VPC and the background which creates a well-defined Dirac dispersion near the *K* point[3]. First, we determine the bandwidth of interest ranging (shaded in green in Fig. S1) and sweep a to ensure the position of the Dirac point is in the interested band (Fig. S1(f)). To optimize the structure for aligning the bandgap with the interested working bandwidth, we swept Δd to broaden the bandwidth, as depicted in Figs. S1(b-d). Finally, we enlarge the d_1 ($0.519a$) and reduce d_2 ($0.156a$) to form VPC1. The corresponding band structure is shown in Fig. S1(e). VPC2 is the mirror image of VPC1 (see Manuscript Fig. 2(a)).

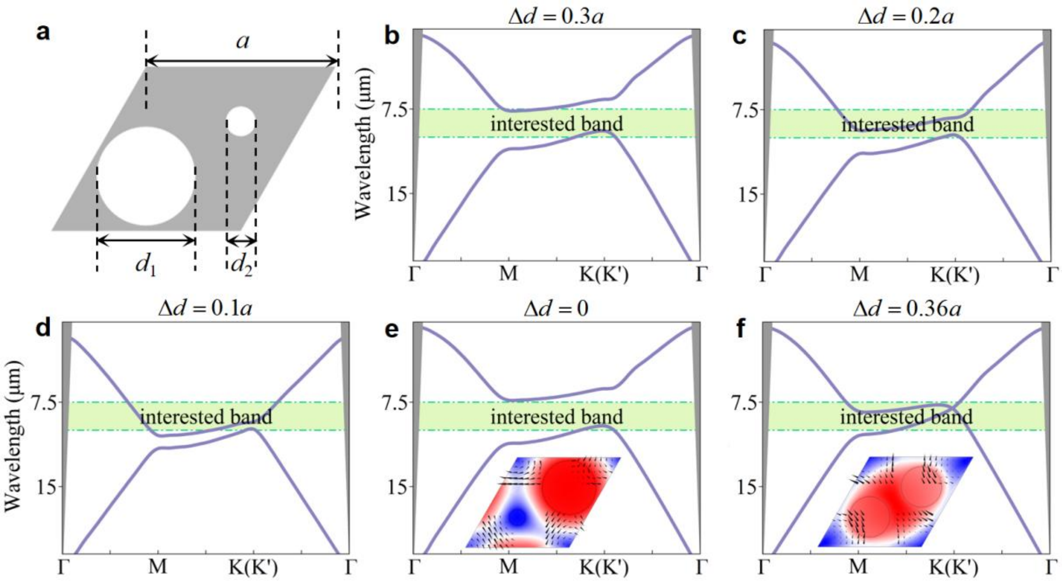

Fig. S1 Geometric optimization of the VPCs. (**a**) The unit cell of the VPCs with two sets of circular air holes, where a is the lattice constant. d_1 and d_2 denote the diameters of air holes. (**b-d**) The parameter sweeping of band structures corresponds to a and Δd. The interested working bandwidth is shaded in green. (**e**) The structure implements the maximum overlap between the working bandwidth and the bandgap. The inset shows the mode profiles of the magnetic field, and the black arrows denote the Poynting vector. (**f**) The honeycomb structure with C_{6v} symmetry generates the Dirac cone at the K valley in the reciprocal space, located within the interested band. The inset shows the mode profiles at the K valley of the magnetic field, and the black arrows denote the Poynting vector.

A more precise optimization allows us to find the eventual parameters where the output heat flux is maximum within the desired band. We calculate the integral of transmission efficiency and input radiation power for different structures to optimize the output heat flux (see Manuscript Figs. 3(j) and (k)). The final optimized structure can achieve the maximum heat flux in the specific bandwidth. Besides, the VPCs structure can conduct further optimization according to actual bandwidth requirements for different applications.

Supplementary Section 2: Band structure calculation of VPCs

Here, we present a derivation of the evolution of eigenfrequency at the K valley based on the Maxwell's equations. We calculate the band structure of the VPCs using the PWE method[4]. By applying Bloch's theorem, we expand the electromagnetic and dielectric functions in the form of plane wave superposition and substitute them into Maxwell's equations to obtain a set of eigenvalues. The VPCs are isotropic and are placed in the passive space, Maxwell's equations can be written as

$$\nabla \times \vec{E} = -\left(\frac{\partial \vec{B}}{\partial t} + \vec{J}_m\right), \tag{1}$$

$$\nabla \times \vec{H} = \frac{\partial \vec{D}}{\partial t} + \vec{J}, \tag{2}$$

where $\vec{B}$, $\vec{D}$, $\vec{E}$, $\vec{H}$ denote magnetic induction vector, inductance intensity vector, electric field intensity vector and magnetic field intensity vector, respectively. The vector $\vec{J}$ and $\overrightarrow{J_m}$ represent the electric and magnetic density, reflecting the electric and magnetic loss.

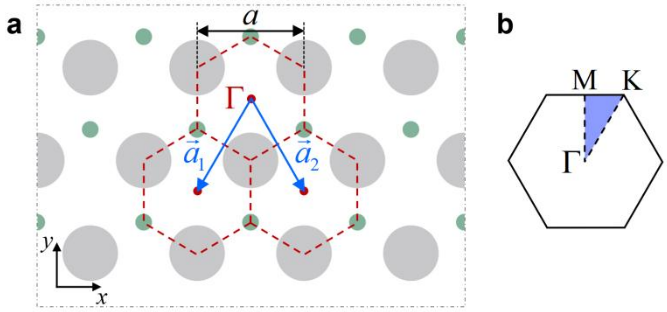

Fig. S2 Schematic of the VPCs in the reciprocal space. (**a**) The corresponding reciprocal lattice. The blue arrows represent the reciprocal vectors. (**b**) The 2D Brillouin zones for each unit cell. The region shaded in purple denotes the first Brillouin zone at the *K* valley.

To make the polarization suitable for our topological waveguide, we only derive the electric field of the transverse-electric (TE) mode, which can be written as

$$\vec{H}(\vec{r},t) = \left(0,0,H_z(\vec{r})\right)e^{-i\omega t}, \tag{3}$$

$$\vec{E}(\vec{r},t) = \left(E_x(\vec{r}),E_y(\vec{r}),0\right)e^{-i\omega t}, \tag{4}$$

where $\vec{r} = x\vec{e}_x + y\vec{e}_y$, and ω is the eigenfrequency. Inserting equation (3) and (4) into equation (1) and (2), we can obtain the equation for H_z

$$\frac{\partial}{\partial x}\left[\frac{1}{\varepsilon(\vec{r})}\frac{\partial H_z}{\partial x}\right] + \frac{\partial}{\partial y}\left[\frac{1}{\varepsilon(\vec{r})}\frac{\partial H_z}{\partial y}\right] + \frac{\omega^2}{c^2}H_z = 0, \tag{5}$$

where $\varepsilon(\vec{r})$ is the relative dielectric constant distributed by period and c is the speed of light. The electromagnetic field satisfies Bloch's theorem and we can expand $\varepsilon(\vec{r})$ and $H_z(\vec{r})$ using the PWE method as

$$\frac{1}{\varepsilon(\vec{r})} = \sum_{\vec{G}}\xi(\vec{G})e^{(i\vec{G}\cdot\vec{r})}, \tag{6}$$

$$H_z(\vec{r}) = \sum_{\vec{G}}h(\vec{k},\vec{G})e^{i(\vec{k}+\vec{G})\cdot\vec{r}}, \tag{7}$$

where $\xi(\vec{G}) = \frac{1}{V}\int\frac{1}{\varepsilon(x,y)}e^{(-i\vec{G}\cdot\vec{r})}dxdy$, and V denotes the area of the unit cell. The reciprocal-lattice vectors $\vec{G}$ are defined as $\vec{G} = h_1\vec{a}_1 + h_2\vec{a}_2$, where $h_1, h_2 \in \mathbb{Z}$ and $\vec{a}_1, \vec{a}_2$ denote the primitive reciprocal-lattice vectors. Vector $\vec{k}$ is the specific wave vectors in the first Brillouin zone and defined as $\vec{k} = k_x\vec{e}_x + k_y\vec{e}_y$. Inserting equation (6) and (7) into equation (5), the eigenequation of $h(\vec{k},\vec{G})$ can be written as

$$h(\vec{k},\vec{G}) = \frac{c^2}{\omega^2}\sum_{\vec{G}}(\vec{k}+\vec{G})(\vec{k}+\vec{G}')\,\xi(\vec{G}-\vec{G}')h(\vec{k},\vec{G}'). \tag{8}$$

The structure of the VPCs is illustrated in Fig. S2. We only consider three waves of PWE expansion that contains the following reciprocal vectors $\vec{G}_0 = 0$ $(h_1 = h_2 = 0)$, $\vec{G}_1 = \vec{a}_1$ $(h_1 = 1, h_2 = 0)$ and $\vec{G}_2 = \vec{a}_2$ $(h_1 = 0, h_2 = 1)$. The vectors $\vec{a}_1$ and $\vec{a}_2$ are defined as $\vec{a}_1 = \left[-\frac{1}{2}, -\frac{\sqrt{3}}{2}\right] a$ and $\vec{a}_2 = \left[\frac{1}{2}, -\frac{\sqrt{3}}{2}\right] a$. By solving the equation (6) and equation (8), we obtain the band structure of the VPCs shown in Fig. 2(b) in the main text.

Supplementary Section 3: Broadband topological edge states propagation

In this section, we demonstrate the simulation results of the topological edge states propagation. The valley-dependent edge state can be achieved by breaking the mirror symmetry of the periodic two-dimensional photonic crystals. Therefore, the topologically-protected valley kink states emerge at the interfaces between two kinds of valley-Hall crystals with opposite Chern numbers, supporting unidirectional and robust transmission owing to the spin-valley locking effect[5]. Here, the calculated structure is periodic in the *x*-direction with 20 unit cells and is finite in size along the *y*-direction. Here, the two topological structures (see Main text Fig. 2(a)) form the boundary to support edge states. In our VPC structure, the boundaries are presented as AB interface and BA interface, respectively, as shown in Figs. S3(a) and (b). Figs. S3(c) and (d) show the projected band diagram of the AB and BA interface supercell. The schematic shows the opposite group velocity and propagation direction of edge states both at *K* and *K'* and different interfaces (AB and BA)[4].

The difference between the two structures is the valley Chern numbers across the domain wall, which is given by $\Delta C^{K}_{\mathrm{VPC1}} = \frac{1}{2}$, $\Delta C^{K'}_{\mathrm{VPC1}} = -\frac{1}{2}$ for AB interface and $\Delta C^{K}_{\mathrm{VPC2}} = -\frac{1}{2}$, $\Delta C^{K'}_{\mathrm{VPC2}} = \frac{1}{2}$ for BA interface[6]. The corresponding specific dots (in blue and red) are shown in Fig. 2(c) in the main text, indicating the designed structure. The corresponding normalized electric field distribution is shown in Figs. S3(e) and (f), and the profile is mirror symmetric regarding the x-axis (y = 0).

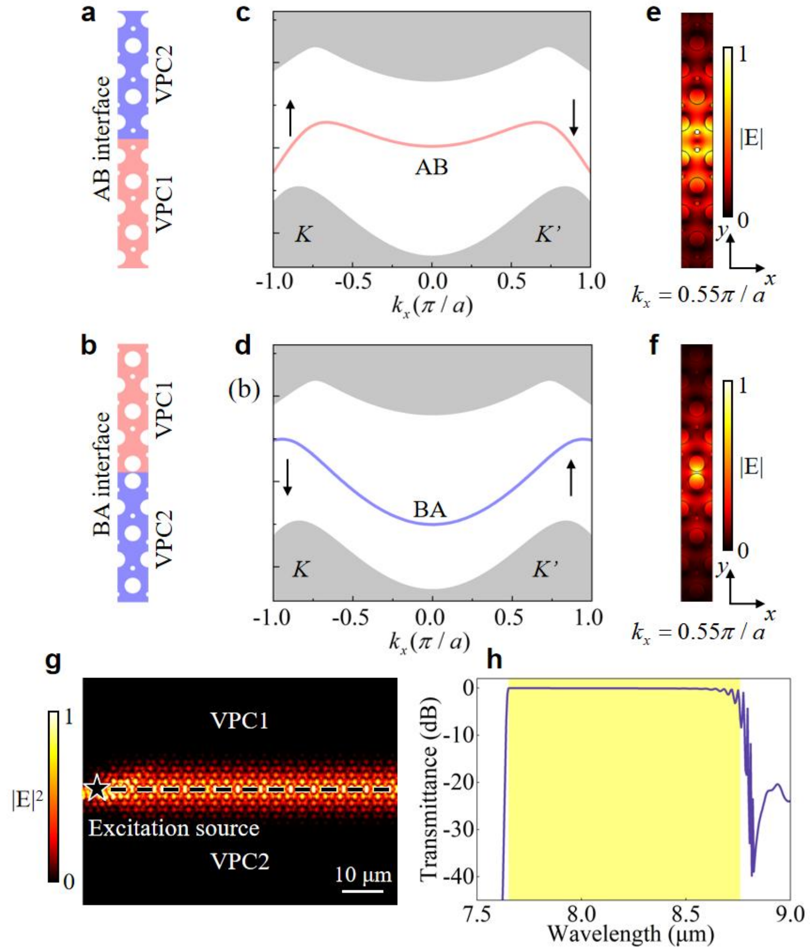

Fig. S3 Topological edge states in VPCs. (**a**), (**b**) The schematic for the asymmetric AB interface and BA interface along the *x*-direction, with purple and pink regions indicating VPC1 and VPC2, respectively. (**c**), (**d**) Band diagrams for the supercell representing the AB interface edge state (pink line) and BA interface edge state (purple line), respectively. The gray regions denote the bulk states, and k_x indicates the wavevector along the boundary. (**e**), (**f**) The normalized electric field distribution for the edge states of structures corresponds to structures shown in (**a**), (**b**). (**g**) The normalized in-plane electric field intensity distribution of BA interface at 7.84 μm. The black star marks the excitation source, and the black dashed line represents the boundary constructed by the two VPCs with opposite Chern numbers. (**h**) The transmittance spectrum of a straight waveguide and the working bandwidth is shaded in yellow.

Further, we compared the two kinds of boundaries using distinct input waveguides (see Figs. 3(a) and (c) in the main text) to demonstrate the unidirectional transmission property. The BA interface shows excellent temperature-independent transmission (see Figs. 3(d) and (f) in the main text) and efficient heat transfer (see Figs. S3(g) and (h)). The normalized energy-density distribution along the straight topological waveguide is depicted in Fig. S3(g), where an electric dipole is placed on the left input port as the excitation source. The transmittance is illustrated in Fig. S3(h) and shows a near-unity value in the working band. For the mid-gap modes from 7.618-8.727 μm (shaded in yellow), the edge states can propagate through the waveguide with high transmittance.

Supplementary Section 4: The temperature-independent transmission via the silicon-based VPCs

In this section, we illustrate the principle of temperature-independent transmission and the temperature distribution of the VPCs. The material of the VPCs is chosen for several reasons to fulfill the desired requirements. Firstly, to dissipate heat via the VPC platform, we consider a vacuum environment to avoid the effects of heat conduction and convection. The material should not absorb in the IR wavelength region to avoid being heated by thermal radiation. Besides, silicon is suitable for nanofabrication and compatible with integrated photonic and electronic devices.

Notably, the absorption coefficient (α) and extinction coefficient (k) of silicon are related to the temperature of the VPCs. To further verify the temperature distribution, we check the value of k in the working band and α corresponding to Beer-Lambert law. The result indicates that the radiation absorbed by the VPCs is negligible in the working band. In addition, the refractive index remains stable in the working band as well as various temperatures, and the approximate value is 3.416 which is consistent with the simulation settings.

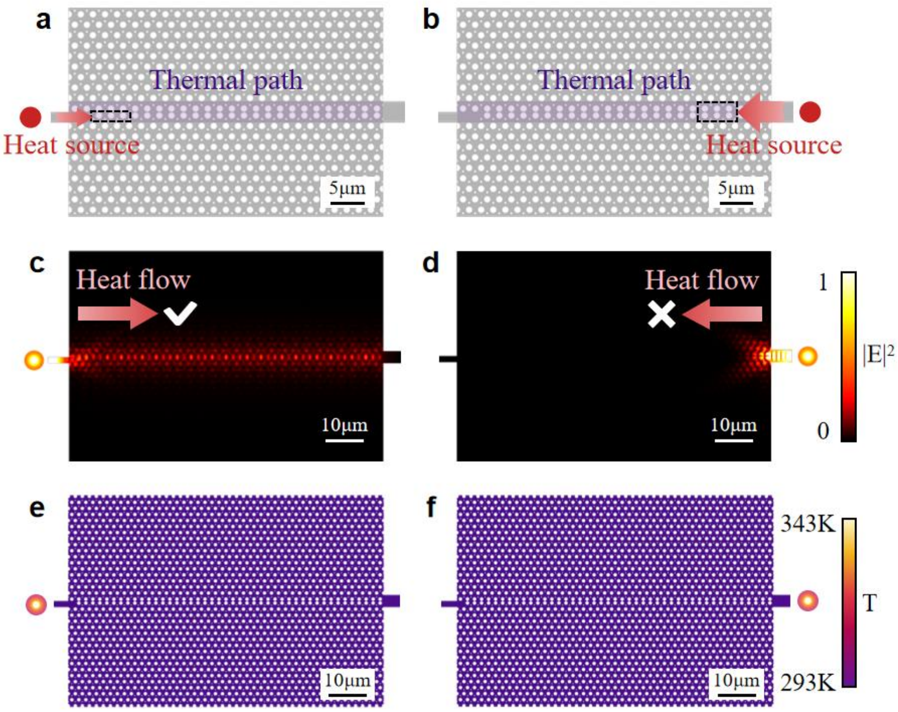

Fig. S4 Temperature-independent heat transfer. (**a**), (**b**) The structral schematics of waveguides with different input ridge waveguides (see Figs. 3(**a**) and (**c**) in the main text). The purple-shaded regions denote the heat transfer path. (**c**), (**d**) The electric field intensity distribution with a single heat source shows high-efficiency and blocked heat transfer, respectively. (**e**), (**f**) The temperature distribution corresponding to the structures in (**a**), (**b**). The VPCs exhibit the same as the ambient temperature.

In order to visualize the radiation heat transfer, we perform the simulation with a single heat source placed at different input waveguides. The left ridge waveguide in Fig. S4(a) is aligned with a row of circular air holes at the boundary, which can support high-efficiency heat transfer, as depicted in Fig. S4(c). While the right waveguide is wider and aligned to the center of the boundary, as shown in Fig. S4(b), which shows a low heat transfer efficiency (Fig. S4(d)) as the heat flux is blocked at the entrance, achieving unidirectional transmission. Figs. S4(e) and (f) depict the corresponding temperature distributions. The results indicate that the heat transfer direction is solely determined by the structures of input waveguides rather than the temperature of the heat source. As a result, in the case of two heat sources on both sides, the heat from a lower-temperature source can transfer to a higher-temperature source (see Figs. 3(b) and (e) in the main text). We assume the ambient temperature is 293 K and the maximum temperature of the heat source is 343 K. The result shows that the VPCs are not heated up during the transmission, and the effect of heat conduction on the transmission efficiency can be ignored. Therefore, the VPC platform implements temperature-independent heat transfer and is particularly useful for devices with significant temperature fluctuation in a short time. The merits listed above make silicon-based VPCs an ideal platform for radiative thermal dissipation.

Supplementary Section 5: Radiative and conductive heat transfer derivation

In this section, we analyze the ultrafast radiative heat transfer and traditional conductive heat transfer characteristics of the VPCs. Different from the slow conductive heat transfer that imposes severe limitations on heat transfer of on-chip integrated devices, thermal radiation is ultrafast and transmitted in the form of electromagnetic waves. We use the finite-difference time-domain (FDTD) method to solve for spatial electromagnetic fields in a stepwise progression on the time axis[7].

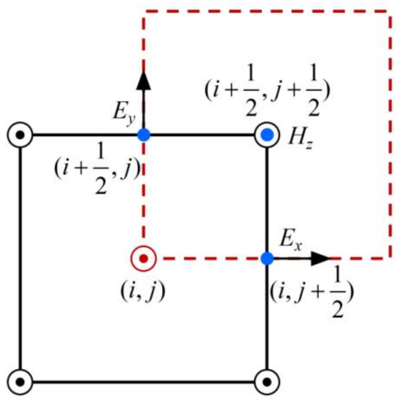

Fig. S5 Two-dimensional Yee cell of the TE wave. The blue dots denote electromagnetic field components to be calculated.

Converting Maxwell's equations given in equation (1) and equation (2) into scalar equations for the TE case in rectangular coordinates yields

$$\begin{cases} \frac{\partial H_z}{\partial y} = \varepsilon \frac{\partial E_x}{\partial t} + \sigma E_x \\ -\frac{\partial H_z}{\partial x} = \varepsilon \frac{\partial E_y}{\partial t} + \sigma E_y \\ \frac{\partial E_y}{\partial x} - \frac{\partial E_x}{\partial y} = -\mu \frac{\partial H_z}{\partial t} - \sigma_m H_z \end{cases}, \quad (9)$$

where ε denotes the dielectric constant, μ denotes the magnetic permeability, σ denotes the electrical conductivity and σ_m denotes the magnetoresistance. Further, the rectangular difference grids are created in the region space and allow $f(x,y,z,t)$ to represent the components of $\vec{E}$ and $\vec{H}$ at any point, the expression in time and space can be written as

$$f(x,y,z,t) = f(i\Delta x, j\Delta y, k\Delta z, n\Delta t) = f^{''}(i,j,k). \quad (10)$$

The first-order partial derivatives of equation (10) with respect to time and space by taking the central difference can be discretized using Yee unit cell in Fig. S5 as

$$\begin{cases} \frac{\partial f}{\partial x}|x = i\Delta x \approx \frac{1}{\Delta x}[f^n(i+\frac{1}{2},j,k) - f^n(i-\frac{1}{2},j,k)] \\ \frac{\partial f}{\partial y}|y = j\Delta y \approx \frac{1}{\Delta y}[f^n(i,j+\frac{1}{2},k) - f^n(i,j-\frac{1}{2},k)] \\ \frac{\partial f}{\partial z}|z = k\Delta z \approx \frac{1}{\Delta z}[f^n(i,j,k+\frac{1}{2}) - f^n(i,j,k-\frac{1}{2})] \\ \frac{\partial f}{\partial t}|t = n\Delta t \approx \frac{1}{\Delta t}[f^{n+\frac{1}{2}}(i,j,k) - f^{n-\frac{1}{2}}(i,j,k)] \end{cases}. \quad (11)$$

In solving Maxwell's equations using the FDTD method, the equations containing time-varying quantities in Yee's grid are first converted into difference equations. Then the electric and magnetic field components at each point of the grid space are calculated at each time step. With the recurrence of time steps, the transmission mode of electromagnetic waves and their interaction process with the medium can be directly calculated. The Yee cell of the TE wave is depicted in Fig. S5. Each field component is surrounded by four field components which yield

$$E_x^{n+1}(i+\frac{1}{2},j) = X(s)E_x^n(i+\frac{1}{2},j) + Y(s)\frac{1}{\Delta y}\left(H_z^{n+\frac{1}{2}}(i+\frac{1}{2},j+\frac{1}{2}) - H_z^{n+\frac{1}{2}}(i+\frac{1}{2},j-\frac{1}{2})\right), \quad (12)$$

where $s = i+\frac{1}{2},j$.

$$E_y^{n+1}(i,j+\frac{1}{2}) = X(s)E_y^n(i,j+\frac{1}{2}) - Y(s)\frac{1}{\Delta x}\left(H_z^{n+\frac{1}{2}}(i+\frac{1}{2},j+\frac{1}{2}) - H_z^{n+\frac{1}{2}}(i-\frac{1}{2},j+\frac{1}{2})\right), \quad (13)$$

where $s = i,j+\frac{1}{2}$.

$$H_z^{n+\frac{1}{2}}(i+\frac{1}{2},j+\frac{1}{2}) = P(s)H_z^{n-\frac{1}{2}}(i+\frac{1}{2},j+\frac{1}{2}) \\ -Q(s)\left(\frac{E_y^n(i+1,j+\frac{1}{2}) - E_y^n(i,j+\frac{1}{2})}{\Delta x} - \frac{E_x^n(i+\frac{1}{2}j+1) - E_x^n(i+\frac{1}{2}j)}{\Delta y}\right), \quad (14)$$

where $s = i + \frac{1}{2}, j + \frac{1}{2}$ and $X(s)$, $Y(s)$, $P(s)$, $Q(s)$ are defined as

$$X(s) = \frac{\frac{\varepsilon(s)}{\Delta t} - \frac{\sigma(s)}{2}}{\frac{\varepsilon(s)}{\Delta t} + \frac{\sigma(s)}{2}} = \frac{1 - \frac{\sigma(s)\Delta t}{2\varepsilon(s)}}{1 + \frac{\sigma(s)\Delta t}{2\varepsilon(s)}}, \tag{15}$$

$$Y(s) = \frac{1}{\frac{\varepsilon(s)}{\Delta t} + \frac{\sigma(s)}{2}} = \frac{\frac{\Delta t}{\varepsilon(s)}}{1 + \frac{\sigma(s)\Delta t}{2\varepsilon(s)}}, \tag{16}$$

$$P(s) = \frac{\frac{\mu(s)}{\Delta t} - \frac{\sigma_m(s)}{2}}{\frac{\mu(s)}{\Delta t} + \frac{\sigma_m(s)}{2}} = \frac{1 - \frac{\sigma_m(s)\Delta t}{2\mu(s)}}{1 + \frac{\sigma_m(s)\Delta t}{2\mu(s)}}, \tag{17}$$

$$Q(s) = \frac{1}{\frac{\mu(s)}{\Delta t} + \frac{\sigma_m(s)}{2}} = \frac{\frac{\Delta t}{\mu(s)}}{1 + \frac{\sigma_m(s)\Delta t}{2\mu(s)}}. \tag{18}$$

Combining equations (15-18) with equations (12-14), we can obtain the electric field distribution at different times that exhibits ultrafast radiative heat transfer within femtosecond timescales (see Main text Fig. 4(a-c)).

To represent how heat is transferred within a material over time, we analyze the heat conduction process to obtain the temperature distribution. We use the finite element method (FEM) to calculate the differential equation for heat conduction numerically[8]. The method discretizes the domain into a finite number of small elements. The temperature distribution within each element is approximated using a set of mathematical functions. It is combined to form a system of equations, which is solved using FEM to obtain an approximation of the temperature distribution within the object. The differential equation for heat conduction can be written as

$$\rho C \frac{\partial T}{\partial t} - \nabla \cdot (\kappa \nabla T) = Q, \tag{19}$$

where T is the object's temperature, t is the transmission time, and Q is the energy generation rate. ρ, C and κ represent mass density, heat capacity, and thermal conductivity, respectively. It should be noted that this equation is only applicable to heat conduction in special cases such as no radiation and no convection. The calculated temperature distribution for conductive heat transfer under different transmission times is shown in the Main text Fig. 4(g-i), exhibiting low transmission efficiency and longer time than radiative heat transfer.

Supplementary Section 6: Heat transfer path design and defect immune heat transfer

The spin-valley locking effect makes the heat flux transfer along the boundary robust against sharp bends, defects, and impurities. In this way, the VPC platform can manipulate the heat flow at will, thus stimulating more unique structures created under various conditions. We demonstrate the heat transfer performance against sharp bends. The structure design and electric field intensity distributions are depicted in Figs. S6(a) and (b). Besides, in order to quantitatively prove the characteristics of defect immunity, we introduce two types of defects and calculate the transmittance of the propagation. The structure diagram of defect type 1 is shown in Fig. S6(d), deleting one large circular air hole at the boundary, which still shows robust transmission. The normalized electric field intensity distribution is depicted in Fig. S6(e). Another type of defect and the corresponding electric field intensity distribution are shown in Figs. S6(g) and (h). The transmittance spectra of these waveguides are shown in Figs. S6(c), (f), and (i).

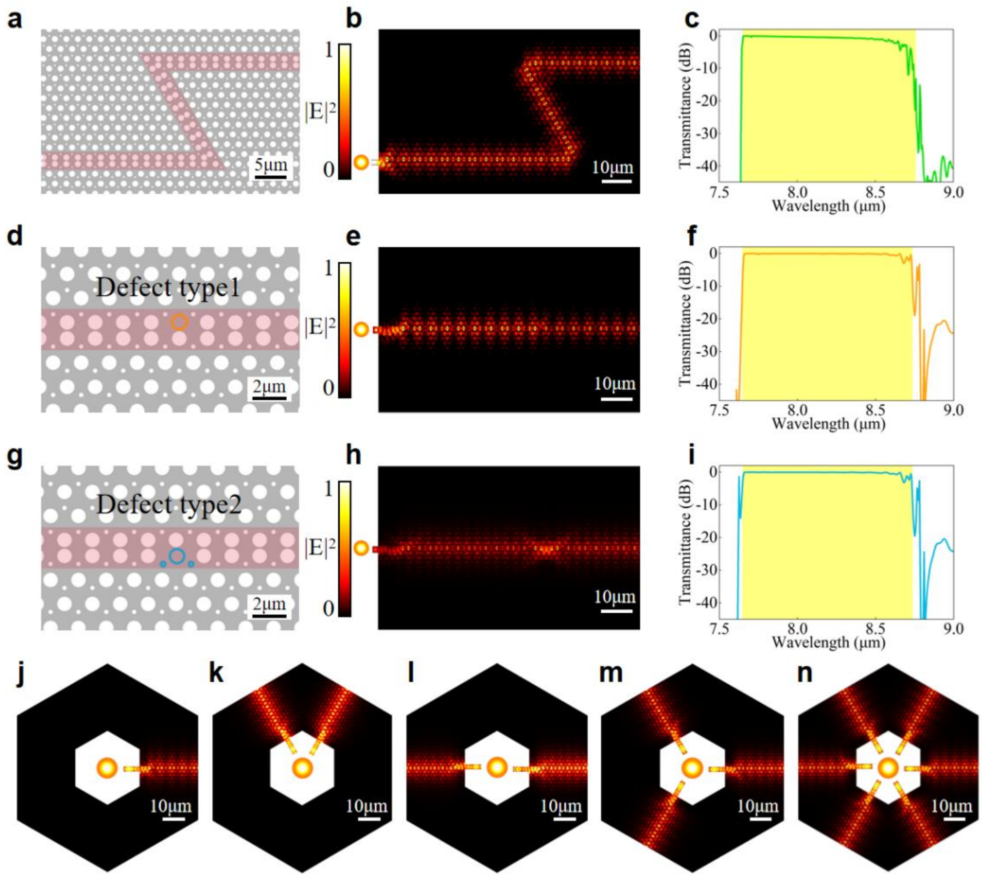

Fig. S6 Defect-immunity and arbitrary path control of VPCs. (a) The structural schematic of Z-shape waveguide with two sharp bends marked by the pink shaded region. **(b)** The corresponding electric field intensity distributions. **(c)** The corresponding transmittance spectrum, and the working bandwidth is shaded in yellow. **(d)**, **(g)** The schematics of VPCs missing one large circular air hole (defect type1, marked by the orange circle) and missing one large and two small circular air holes (defect type2, marked by the blue circles) at the boundary. **(e)** and **(h)** The electric field intensity distributions corresponding to the defect type1 and type2, respectively. **(f)** and **(i)** The transmittance spectra corresponding to the defect type1 and type2, respectively. **(j)-(n)** Electric field intensity distributions of multi-channel heat dissipation structures with different numbers of channels.

The simulated results show the great potential of the VPC platform for thermal dissipation, breaking the constraints of conventional methods that exhibit a significant decrease in heat transfer when encountering fabrication defects and sharp bends. Furthermore, we design several suitable structures to dissipate more heat from the source and investigate the factors affecting thermal dissipation efficiency, including the channel numbers and angle between channels.

Each channel contains 12 unit cells in a row. The diameter of the heat source is 10 μm and the input waveguides are 12 μm in length. The related electric field intensity distributions are illustrated in Figs. S6(j)-(n), and the quantitative comparison of the heat dissipation with different numbers of channels is also studied (see Fig. 5(i) in the main text). The results indicate that the increase in the number of thermal paths will expand the source's heat dissipation area, thereby improving heat transfer efficiency.

Supplementary Section 7: Design of suitable heat source

Radiative emission is in all directions, and how to couple the thermal radiation to the waveguide is critical to ensure high cooling efficiency. To compensate for the strict light mode and direction requirements, we specially design the heat source structure utilized in our work. As depicted in Fig. S7, we create a parabolic mirror surrounding the heat source. The diffusive thermal radiation from the source will be reflected by the parabolic mirror and focused by the lens to the input waveguide. Therefore, the radiative heat flow could be transmitted to the heat sink with negligible loss, thus realizing ultrafast and efficient heat transfer based on the VPCs.

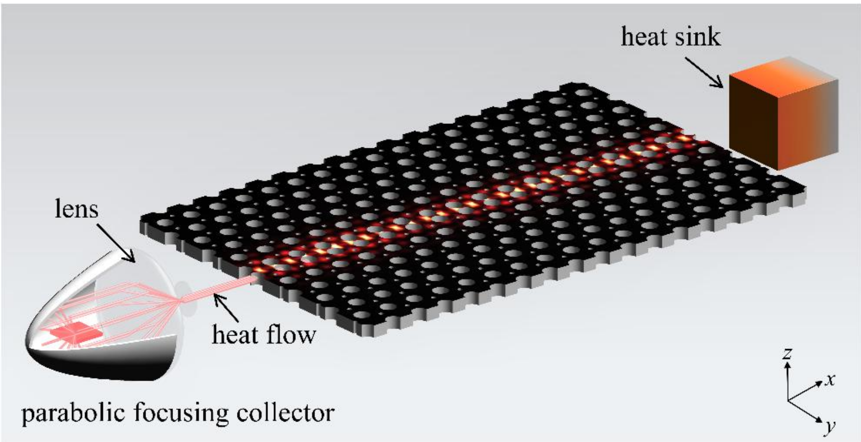

Fig. S7 A parabolic mirror covers a heat source and focuses on the input waveguide by the lens.

Reference

1. L. Lu, J. D. Joannopoulos & M. Soljacic·Topological photonics.·*Nat. Photonics*·**8,**·821-829·(2014).
2. X. T. He, et al.·A silicon-on-insulator slab for topological valley transport.·*Nat. Commun.*·**10,**·872·(2019).
3. Z. Zhang, et al.·Azimuthally and radially polarized orbital angular momentum modes in valley topological photonic crystal fiber.·*Nanophotonics*·**10,**·4067-4074·(2021).
4. K. M. Ho, C. T. Chan & C. M. Soukoulis·Existence of a photonic gap in periodic dielectric structures.·*Phys. Rev. Lett.*·**65,**·3152-3155·(1990).
5. Y. H. Kang, X. Ni, X. J. Cheng, A. B. Khanikaev & A. Z. Genack·Pseudo-spin-valley coupled edge states in a photonic topological insulator.·*Nat. Commun.*·**9,**·(2018).
6. M. I. Shalaev, W. Walasik, A. Tsukernik, Y. Xu & N. M. Litchinitser·Robust topologically protected transport in photonic crystals at telecommunication wavelengths.·*Nat. Nanotech.*·**14,**·31-34·(2019).
7. A. Rivas & M. A. Martin-Delgado·Topological Heat Transport and Symmetry-Protected Boson Currents.·*Sci Rep*·**7,**·(2017).
8. B. J. Gireesha, G. Sowmya & M. Macha·Temperature distribution analysis in a fully wet moving radial porous fin by finite element method.·*Int. J. Numer. Methods Heat Fluid Flow*·**32,**·453-468·(2022).